

Geochemistry, Geophysics, Geosystems®



RESEARCH ARTICLE

10.1029/2022GC010789

Key Points:

- A ferromanganese nodule of the South Pacific showed stable magnetizations, whose directions form a great circle suggesting rotation with time
- The major magnetic mineral is magnetite, and its oxidation to maghemite may have caused acquisition of secondary magnetization during rotation
- Rotation is important for the chemistry of nodules as it permits the growth of a mixed layer with diagenetic buserite and hydrogenetic vernadite

Supporting Information:

Supporting Information may be found in the online version of this article.

Correspondence to:

H. Oda,
hirokuni-oda@aist.go.jp

Citation:

Oda, H., Katanoda, W., Usui, A., Murayama, M., & Yamamoto, Y. (2023). Rotation of a ferromanganese nodule in the Penrhyn Basin, South Pacific, tracked by the Earth's magnetic field. *Geochemistry, Geophysics, Geosystems*, 24, e2022GC010789. <https://doi.org/10.1029/2022GC010789>

Received 14 NOV 2022

Accepted 19 JAN 2023

Corrected 17 JUN 2023

This article was corrected on 17 JUN 2023. See the end of the full text for details.

Author Contributions:

Conceptualization: Hirokuni Oda, Akira Usui, Masafumi Murayama




Data curation: Hirokuni Oda, Wataru Katanoda

Formal analysis: Hirokuni Oda, Wataru Katanoda, Yuhji Yamamoto

© 2023 The Authors.

This is an open access article under the terms of the [Creative Commons Attribution-NonCommercial License](https://creativecommons.org/licenses/by-nc/4.0/), which permits use, distribution and reproduction in any medium, provided the original work is properly cited and is not used for commercial purposes.

Rotation of a Ferromanganese Nodule in the Penrhyn Basin, South Pacific, Tracked by the Earth's Magnetic Field

Hirokuni Oda¹ , Wataru Katanoda^{1,2}, Akira Usui³, Masafumi Murayama^{2,3} , and Yuhji Yamamoto³ 

¹Geological Survey of Japan, AIST, Tsukuba, Japan, ²Graduate School of Integrated Arts and Science, Kochi University, Kochi, Japan, ³Center for Advanced Marine Core Research, Kochi University, Kochi, Japan

Abstract Ferromanganese nodules are cm-sized, authigenic, abyssal manganese-iron-hydroxide concretions. They grow very slowly at rates of a few mm per million years. Although their ages are older than millions of years, they are often found half buried on the modern sediment surface. The mechanisms for the nodules' persistence at the surface without complete burial could be linked to their occasional motion or agitation. Here, we report evidence for the rotation of a nodule from the Penrhyn Basin, South Pacific detected by paleomagnetism. The paleomagnetic inclinations of specimens from the nodules' surface are consistent with the recent geomagnetic fields. The paleomagnetic directions from the surface to the core show successive changes and form a great circle with a pole at (azimuth = 53.9°, dip = 32.1°). This suggests that the nodule rotated along its pole while successively recording magnetizations. As the nodule was found on a gentle slope at the foot of an abyssal hill, it may have moved downslope due to bottom current underwashing. Rock magnetic analyses of the nodule suggest the presence of magnetite in single domain and vortex states. Low temperature magnetometry revealed that magnetite grains were heavily oxidized to maghemite, especially close to the core of the nodule. The rotation may have exposed the rising part of the nodule to oxidative pore water. Oxygenated Antarctic Bottom Water might have caused remagnetization due to low temperature oxidation of magnetite. The rotation would also facilitate the omnidirectional growth of the nodules' mixed layer of diagenetic buserite and hydrogenetic vernadite.

Plain Language Summary Ferromanganese nodules are deep marine mineral resources that grow very slowly at a speed of few mm per million years on the seabed. They are very old, but often remain on the sediment surface. It remains unclear, why they were not buried by deep-sea sedimentation. A nodule recovered from the Penrhyn Basin in the South Pacific was measured to reveal its fossil magnetization by the ancient Earth's magnetic field. Each specimen from the nodule showed a stable magnetization that is linearly decreasing toward the origin during alternating field demagnetization. The dip of the magnetization for the surface is consistent with the recent Earth's magnetic field, while the magnetization directions toward the nodule's center form a great circle. This suggests that the nodule rotated along a pole while successively recording magnetizations. The nodule may have moved downslope due to sediment removal by deep current. The rotation may have made the pore water within the nodule more oxidative, causing loss of primary magnetization and acquisition of secondary magnetization by removing Fe²⁺ from magnetite (Fe₃O₄). The rotation of the nodule would also stimulate the growth of its two interlayered mineral phases, of which one grows better in sediment and the other in seawater.

1. Introduction

Marine ferromanganese nodules (nodules, hereafter) are widely found abyssal concretions with concentric layers of manganese-iron-hydroxides, which typically grow at a speed of about few mm/Myr (e.g., Verlaan & Cronan, 2022; von Stackelberg, 2000). These nodules are considered as a future mineral resource of Cu, Ni, Co, and rare earth elements. While such nodules are also found buried in deeper sediments, many of them are still exposed on the sediment surface despite their geologically old age of tens of millions of years (e.g., Verlaan & Cronan, 2022; von Stackelberg, 2000). The nodules are composed of two phases: diagenetic buserite with metal ions in sediment and hydrogenetic vernadite with colloids in seawater (e.g., Skowronek et al., 2021; Usui & Someya, 1997; Usui et al., 1989; Verlaan & Cronan, 2022). Usui and Ito (1994) demonstrated using Ocean Drilling Program cores that buried nodules are usually found in stratigraphic layers corresponding to hiatuses or slow sedimentations. Graham et al. (2004) reported using ¹⁰Be chronology that the surface ages of the buried nodules

Funding acquisition: Hirokuni Oda
Investigation: Hirokuni Oda, Wataru Katanoda, Akira Usui, Masafumi Murayama, Yuhji Yamamoto
Methodology: Hirokuni Oda, Wataru Katanoda, Yuhji Yamamoto
Project Administration: Hirokuni Oda, Akira Usui, Masafumi Murayama
Resources: Hirokuni Oda, Akira Usui, Masafumi Murayama, Yuhji Yamamoto
Supervision: Hirokuni Oda, Akira Usui, Masafumi Murayama
Validation: Hirokuni Oda, Yuhji Yamamoto
Visualization: Hirokuni Oda, Wataru Katanoda
Writing – original draft: Hirokuni Oda, Wataru Katanoda
Writing – review & editing: Hirokuni Oda, Akira Usui, Yuhji Yamamoto

are consistent with the ages for the surrounding sediments and that the buried nodules retain their surfaces after burial. These suggest that the buried nodules had been growing on the sediment surface during slow sedimentations or hiatuses and that their burials are initiated by increases in the sedimentation rates.

Although the growth of the nodules without burial during hiatuses and the burial of the nodules at high sedimentation rates are understandable, it is not easy to develop a model that can explain the growth of the nodules without burial convincingly at low sedimentation rates. Usui (1979) indicated that the nodules could have moved or rotated during growth based on the internal structures of the two phases. von Stackelberg (1984) suggested that the activities of benthic organisms are one of the possible driving forces of the possible movements. Usui and Ito (1994) suggested that the buried fossil manganese nodules are formed under the condition of very slow (<0.5 m/Myr) or no sedimentation (hiatuses) promoted by oxygenated bottom currents as well as the modern nodules exposed on the seafloor. Based on their hypothesis, oxygenated bottom currents may have played a role in the movements of the nodules. However, no direct observations have so far demonstrated the most likely extremely slow or very rare physical movement during their growth.

Paleomagnetism has often provided valuable information on the formation of geological structures. The changing polarity of the Earth's magnetic field is commonly recorded by sedimentary processes enabling the magnetostratigraphic dating of sediment depositional age. For example, paleomagnetic measurements on mm-sized specimens of marine ferromanganese crusts (crusts, hereafter) mainly comprising hydrogenetic vernadite, allowed to establish robust magnetostratigraphic age models of the crust's evolution (Joshima & Usui, 1998; Yuan et al., 2017). Furthermore, scanning superconducting quantum interference device (SQUID) microscopy (Kawai et al., 2016; Oda et al., 2016) was successful in restoring these magnetic polarity sequences even at submillimeter scale. The estimated crust ages were consistent with ^{10}Be chronology (Noguchi et al., 2017; Oda et al., 2011, 2020). Such evidence confirms that crusts are a reliable long-term archive of the Earth's magnetic field. A nodule from the Clarion-Clipperton Zone (CCZ; a red diamond in Figure 1a; Yi et al., 2020) has been suggested to record the Earth's magnetic field successively during growth without rotation based on the undistorted paleomagnetic inclinations. Conversely, the nodule rotation could be detected as paleomagnetic directions, disagreeing with that for a geocentric axial dipole (GAD) field. Here, we report the paleomagnetic results on a nodule from the Penrhyn Basin and discuss the possibility of rotation during growth.

Single domain (SD) magnetite formed by magnetotactic bacteria is a common constituent and magnetization carrier of ferromanganese crust (Oda et al., 2018; Yuan et al., 2020). Fossil magnetosomes of magnetotactic bacteria were also reported for a nodule in the Pacific (Jiang et al., 2020). It is therefore of particular interest to determine the role biogenic magnetite and its alteration products play in the magnetic remanence acquisition of ferromanganese nodules.

2. Samples and Methods

2.1. Geological Setting and Samples

We used a nodule sample from the Penrhyn Basin ($158^{\circ}30.64'\text{W}$, $12^{\circ}00.03'\text{S}$; Water depth: 5,248 m), South Pacific (blue diamond in Figure 1a) collected during the GH83-3 cruise. This sampling site is located ~ 200 km east of the Manihiki Plateau on the northern foot of an abyssal hill (blue diamond in Figure 1b). A deep current originating from Antarctic Bottom Water (AABW) flows northwards east of the Manihiki Plateau (Kawabe & Fujio, 2010; Figure 1a). Nodules in this area are densely distributed over up to 90% of the seabed consisting of pelagic clay with a mean coverage of 57% (Usui et al., 1993). The sediment has been characterized as dark reddish-brown homogeneous zeolite-rich clay (Nishimura & Saito, 1994).

2.2. Sample Treatment and Paleomagnetic Measurements

A box corer was used to collect the studied nodule onto which a white marker was placed to indicate its vertical orientation (Figures 1c and 1d). It has a spheroidal shape with dimensions of $74\text{ mm} \times 60\text{ mm} \times 66\text{ mm}$ (height). Two planar, mutually perpendicular blocks A (thickness: ~ 10 mm) and B (thickness: ~ 10 mm) were cut from the nodule along two vertical planes passing through the marker (Figures 1e–1g). Thin sections were prepared from blocks A and B with thicknesses of 530 and 550 μm , respectively. The remaining parts of blocks A and B are termed Sample-A ($20\text{ mm} \times 30\text{ mm} \times 8\text{ mm}$) and Sample-B ($20\text{ mm} \times 35\text{ mm} \times 9\text{ mm}$),

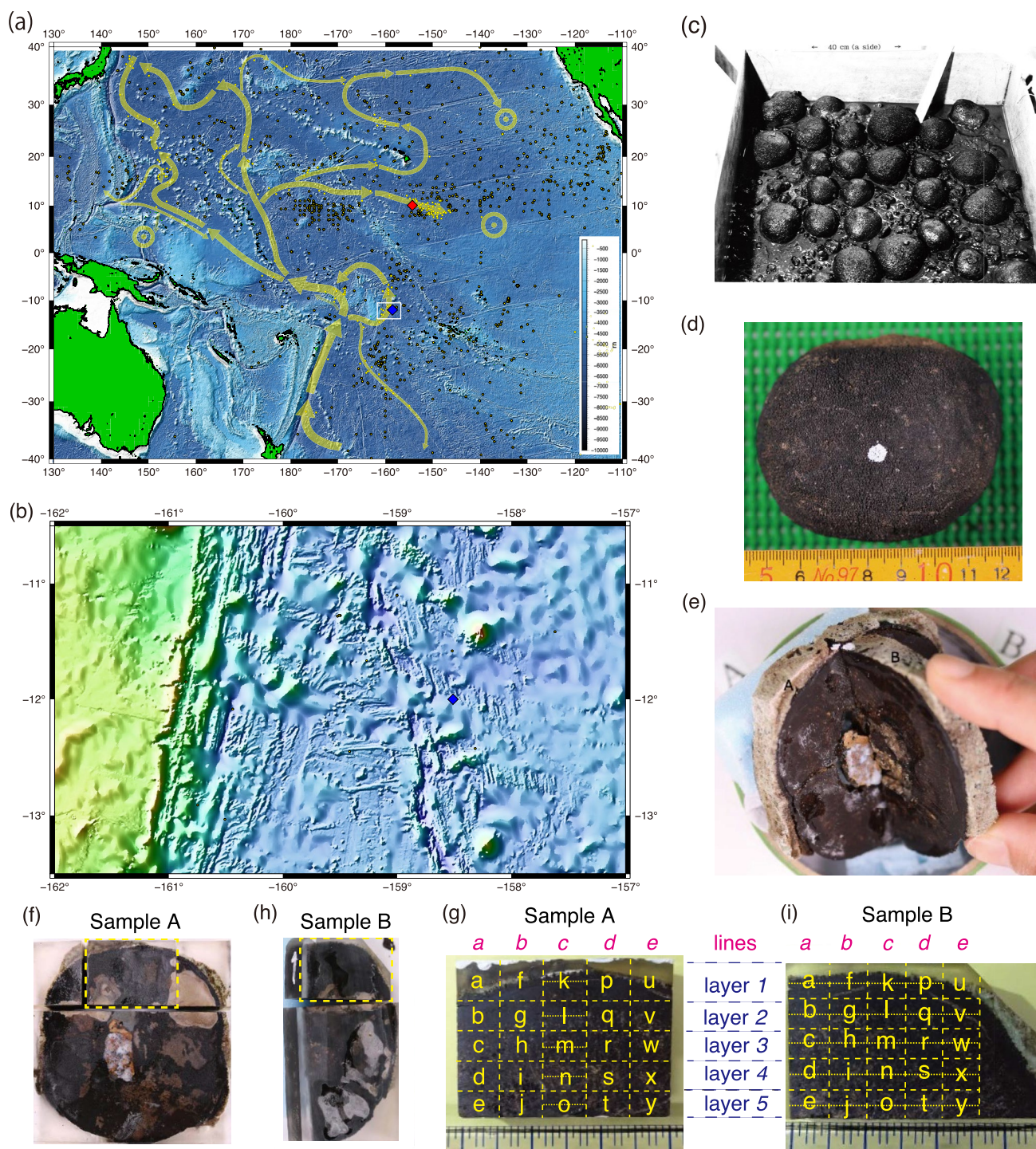


Figure 1. (a) Bathymetric map with nodule sites (yellow dots; Dutkiewicz et al., 2020). Blue and red diamonds are sites of this study and Yi et al. (2020), respectively. Yellow arrows are deep current streamlines (Kawabe & Fujio, 2010). (b) Enlarged map around the sampling site. Bathymetric data of SRTM15 (Tozer et al., 2019) were used with the Generic Mapping Tool version 6 (Wessel et al., 2019). Green represents land and bathymetry is color coded according to the color scale as an inset of panel (a). Mercator projection is used to produce the shaded relief maps with illuminations from the north and west. (c) A box core with the studied nodule. (d) The nodule with a mark at the top. (e) Blocks A and B cut along vertical planes perpendicular to each other. Blocks (f) A and (g) B, which were further cut to make Sample-A and Sample-B (yellow rectangles) for paleomagnetic study, respectively. (h) Sample-A and (i) Sample-B with yellow specimen boundaries. Vertical and horizontal series of specimens are defined as lines, and layers, respectively. Specimens of line *k* for Sample-A and those except *u* for Sample-B were cut into two (orange dotted lines).

respectively. Subsequently, each sample was cut into five subblocks (*a*, *f*, *k*, *p*, *u* lines). Each subblock was cut into 5 (3 mm × 6 mm × 8 mm) or 10 (1.5 mm × 5 mm × 9 mm) specimens with a diamond wire saw at GSJ-Lab (Figures 1h and 1i). Paleomagnetic analyses were performed on the specimens using a superconducting rock magnetometer (SRM model 760R, 2G Enterprises) at GSJ-Lab with stepwise alternating field demagnetization (AFD) up to 80 mT. The paleomagnetic direction for each specimen was obtained using principal component analysis (PCA; Kirschvink, 1980) using “Paleomagnetism.org 2.0” (Koymans et al., 2020).

2.3. Rock Magnetic Analyses

Rock magnetic analyses were conducted on the specimens along line *k* of Sample-A to characterize magnetic minerals. Ten specimens were analyzed on the acquisition of isothermal remanent magnetization (IRM), first order reversal curve (FORC) analysis, and S-ratio ($S_{-0.3T}$ and $S_{-0.1T}$; Bloemendal et al., 1992) using a vibration sample magnetometer (VSM 8604, Lake Shore Inc.). The IRM acquisition curves were measured with an averaging time of 1 s at 200 steps in logarithmic scale starting from 10 μ T up to 2 T, which were unmixed into log-normal coercivity distributions using the *MaxUnmix* software (Maxbauer et al., 2016). First-order reversal curve was processed using the *FORCinel* software (Harrison & Feinberg, 2008).

S-ratios were calculated as part of back field measurements with the VSM. The samples were saturated with 2 T magnetic field and then magnetic moments were measured with an averaging time of 1 s. Subsequently, magnetic moments in zero field were measured after application of the magnetic field at 200 steps on a logarithmic scale starting from -10μ T up to -2 T. Magnetic moments corresponding to -0.1 T and -0.3 T were calculated using interpolation of the obtained data. $S_{-0.3T(-0.1T)}$ is obtained using

$$S_{-0.3T(-0.1T)} = [1 - \text{BIRM}_{-0.3T(-0.1T)} / \text{SIRM}] / 2,$$

where SIRM is the saturation IRM at 2 T, and $\text{BIRM}_{-0.3T(-0.1T)}$ is the IRM at 0.3 T (0.1 T) acquired opposite to SIRM (Bloemendal et al., 1992).

Zero-field-cycling of IRM was conducted on five specimens using the magnetic property measurement system (MPMS) at Kochi Core Center (MPMS-XL5, Quantum Design Inc.). Magnetization was monitored while cooling to 10 K followed by warming to 300 K after exposure to 5 T at 300 K. Measurements were conducted at temperature steps of 1.5 K with a warming or cooling speed of 3 K/min.

Thermal demagnetization of the three-component IRM was performed on specimens *k1* through *o2* for Sample-A based on Lowrie (1990). For each specimen, IRM was imparted with a magnetic field of 2.5 T along the Z-axis using a pulse magnetizer (Model 660; 2G Enterprises) at the GSJ-Lab, AIST. A second IRM was applied at 0.4 T along the Y-axis, followed by a third IRM in a field of 0.12 T along the X-axis. This procedure makes each specimen acquire magnetizations representing its high (0.4–2.5 T), medium (0.12–0.4 T), and low (0–0.12 T) coercivity components by the Z, Y, and X vector components, respectively. Thereafter, all specimens were stepwise thermally demagnetized to detect the unblocking temperatures of the different coercivity intervals.

2.4. Analyses With Optical and XRF Scanner, and Scanning SQUID Microscope

An optical scanner (GT-X980, Seiko Epson Corp.) was used to obtain optical images of thin sections with reflected light at a spatial resolution of 6,400 dpi ($\sim 4 \mu$ m). Compositions of major elements of the thin sections for Sample-A and Sample-B were analyzed using a micro XRF scanner (M4 TORNADO, Bruker Corp.) at GSJ-Lab with an X-ray beam diameter of 25 μ m on 25 μ m grids.

Thin sections were analyzed by scanning SQUID microscopy (SSM) for spatial mapping of the $S_{-0.1T}$ -ratio. The thin section of Sample-A was mapped on a 100 μ m grid using an SSM at AIST (Kawai et al., 2016; Oda et al., 2016). An SIRM was acquired in a field value of 1.2 T with an electromagnet (Model 3470, GMW Associates, Inc.) followed by a back field IRM in a 0.1 T field ($\text{IRM}_{-0.1T}$). Magnetic maps for SIRM and $\text{IRM}_{-0.1T}$ were used to create magnetic moment maps on 200 μ m grids using the inversion software by Weiss et al. (2007). To create the map of $S_{-0.1T}$, we assumed dipole moments at a fixed grid knot distance corresponding to half the thickness of the thin section plus the distance between the sensor and the thin section surface (e.g., Noguchi et al., 2017).

Table 1
¹⁰Be Dating Results for the Studied Nodule

Sample no.	Depth (mm)		¹⁰ Be/ ⁹ Be ($\times 10^{-7}$)	Age (Ma)
	Top	Bottom		
1	0	1	0.93820	0.637
2	3	6	0.10770	4.969
3	9	13	0.05453	6.331
4	20	23	0.02748	7.702

Note. Age is estimated using half life of 1.387 Myr and modern value of 1.29.

2.5. ¹⁰Be/⁹Be Age Determination

For constructing the age model of the studied nodule, four samples were analyzed using cosmogenic nuclide ¹⁰Be by accelerator mass spectrometry at GNS Science, New Zealand (Table 1). Constant flux and a half-life of 1.387 ± 0.012 Myr for ¹⁰Be isotopes (Chmeleff et al., 2010; Korschinek et al., 2010) are assumed to obtain the estimated ages for each sample. The recognized modern value for ¹⁰Be/⁹Be is assumed to be 1.29×10^{-7} based on deep sea value in the Pacific (Oda et al., 2011).

3. Results

3.1. Paleomagnetic Directions

A low coercivity overprint could be removed by AFD at 10 mT (Figure 2). Paleomagnetic directions were obtained by PCA using 4–8 AFD steps giving minimum MAD, which are within the interval between 17.5 and 40 mT (Table S1 in Supporting Information S1) and plotted versus depth. Maximum angular deviations were less than 3° in most cases. Specimens from Sample-A show lower coercivity components with curvatures around ~10 mT (Figure 2a), suggesting that softer coercivity components are partly overlapping with a stable higher coercivity component. We tentatively consider the lower coercivity component of Sample-A to be related to laboratory storage since Sample-A and Sample-B have different storage histories.

All stable paleomagnetic inclinations were negative, suggesting that the magnetizations were acquired during a normal polarity period. Inclinations close to the surface are consistent with the expected inclination for GAD at the site (−23.0°). The inclinations deeper along lines *a*, *f*, *k*, and *p* of Sample-A show steeper negative inclination values (Figure 2c). Inclinations of Sample-B become steeper at medium depth (Figure 2d) and return values close to those from the surface at the bottom of each line. Paleomagnetic declinations along lines *f*, *k*, and *p* of Sample-A are between 90 and 180°, whereas those for lines *a* and *u* differ (Figure 2e). Declinations of Sample-B are ~45° for specimens close to the surface, and gradually change to 150–180° at depth (Figure 2f). A 45° azimuth correction was applied to the declinations of Sample-B assuming that the nodule surface recorded the present GAD field at the site. We tried corrections for the depth of each line relative to the depth for line *k* of each sample based on the growth layers identified with optical and chemical images (Figure S1 in Supporting Information S1). The paleomagnetic directions plotted versus corrected depths (Figures 2e and 2f) did not increase the similarities of the paleomagnetic directions among the five lines. This suggests that the magnetizations were not acquired at the time of growth but at a later time.

3.2. Age Model and Secondary Origin of Magnetization

¹⁰Be chronology is one of the radiometric dating methods for ferromanganese crusts and nodules that can be applied back to ~15 Myr (e.g., Verlaan & Cronan, 2022). For marine ferromanganese crusts, it has been shown that ¹⁰Be chronology is consistent with the magnetostratigraphic dating (Noguchi et al., 2017; Oda et al., 2011, 2020; Yuan et al., 2017). Although, nodule growth is neither regular nor continuous, and diagenetic parts grow faster than hydrogenetic ones (Verlaan & Cronan, 2022), ¹⁰Be chronology could provide a reasonable and continuous age model based on Bayesian modeling in combination with Co-chronology (Jiang et al., 2022). Yi et al. (2020) successfully established an age model for their nodule sample based on ¹⁰Be chronology, which showed agreements with the magnetostratigraphic ages on both sides of the nodule. Based on the above-mentioned perspectives, the ¹⁰Be chronology determines the time of the nodule formation, which should correspond to the acquisition of primary natural remanent magnetization of each layer of the nodule. As our paleomagnetic results do not provide a plausible magnetostratigraphic age model, only a ¹⁰Be chronology was considered reliable and used to establish our age model (Figure 2g).

Notably, the expected time of primary magnetization of specimens *l2* and *n2* falls into the reversed polarity chrons C3n.4r (5.235–6.023 Ma) and C3An.2r (6.727–7.104 Ma), respectively (Ogg, 2020). Assuming sedimentary, biological or chemical magnetization was acquired at the time of growth and the age model is correct, these specimens or others in their surroundings should have acquired reversed polarity magnetization. The complete

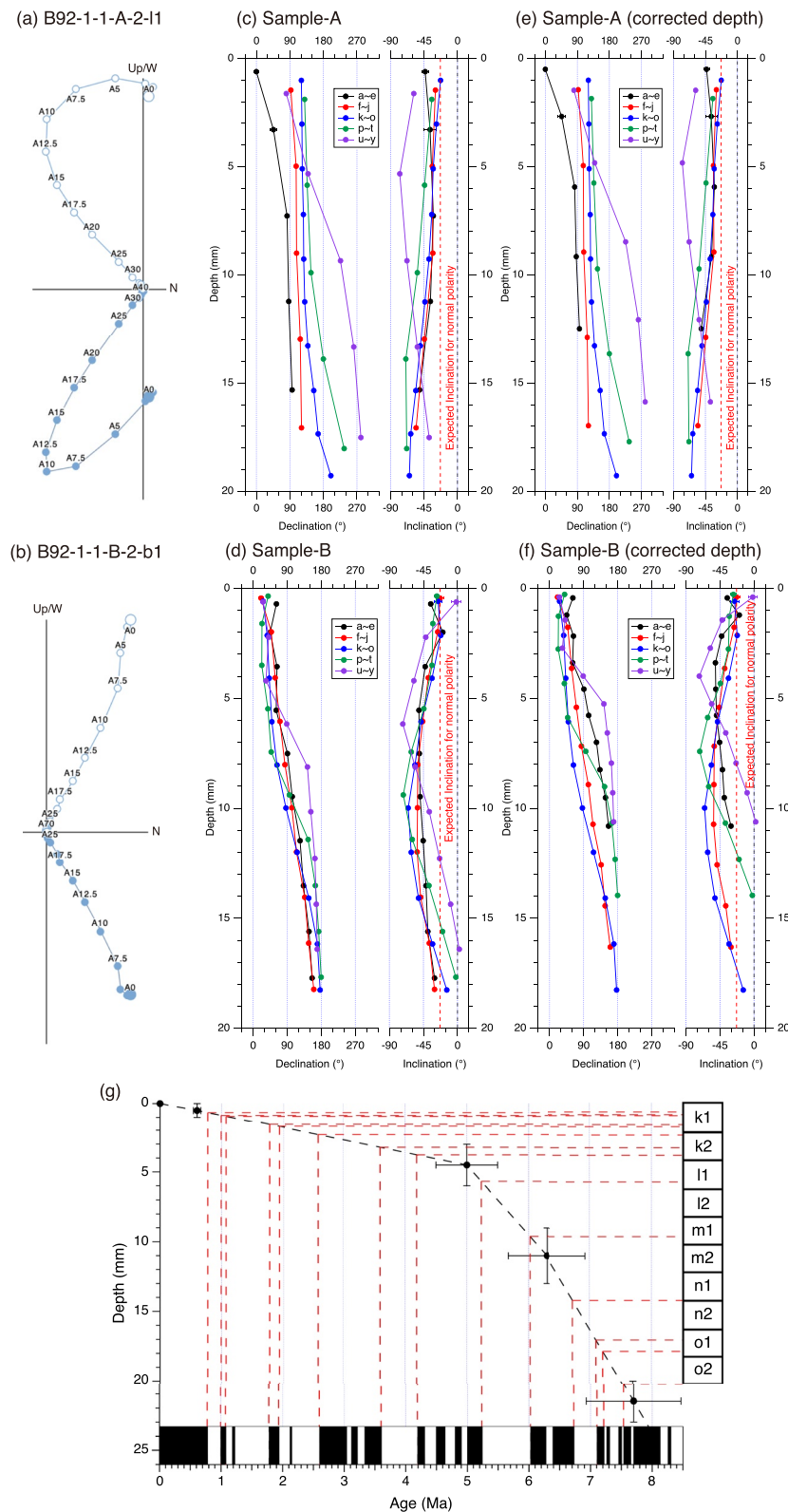


Figure 2.

absence of reversed polarity magnetizations suggests that the nodule was chemically remagnetized during a normal polarity period after its initial growth, presumably during the present Brunhes normal polarity chron (0–0.77 Ma).

3.3. Plate Movement During Growth

The geographic position of the nodule site changed with time as the Pacific Plate moved away from the East Pacific Rise by mid-ocean rifting. The total travel distance of the studied site over the past 8 Myr was about 800 km, corresponding to a latitudinal displacement of about 3° based on plate reconstructions using the GPlates software by Müller et al. (2018). Thus, the latitudinal change of the site is considered negligible in terms of paleomagnetic inclination change, even including the oldest paleomagnetic specimen of ~8 Ma age.

3.4. Rock Magnetism and Magnetic Mineralogy

The results of IRM unmixing (Figure 3) suggest that the nodule's magnetic mineral assemblages contain up to four coercivity components, namely low (C1: ~15 mT), medium (C2: ~38 mT), elevated (C3: ~148 mT), and high (C4: ~850 mT) coercivities. The magnetic mineralogy changes significantly at around 17 mm depth (Figures 3c and 3d). Four coercivity components (C1, C2, C3, and C4) are recognized within 0–17 mm depth, but just two components (C1 and C2) in 17–21 mm depth (specimens *o*1 and *o*2). The absence of C3 (~148 mT) in the 17–21 mm depth section is consistent with its enhanced $S_{-0.1\text{ T}}$ above 0.96 (Figure 8b).

The 10 depicted FORC diagrams in Figure 4 enable us to interpret the domain state and magnetic mineralogy of the specimens (Roberts et al., 2014). There are no obvious features characteristic of MD particles represented by vertical distributions parallel to the B_u axis. There are positive features characteristic of vortex particles around $B_c = 25$ mT and $B_u = -20$ –20 mT. First-order reversal curve diagrams of specimens *o*1 and *o*2 (Figures 5i and 5j) are different from all others with a dominant central ridge extending from $B_c = 0$ up to 80–90 mT and diminishing to zero at 100 mT. The vortex features around $B_c = 25$ mT and $B_u = -20$ –20 mT are quite limited in their distributions without extending further out. C1 for specimens *o*1 and *o*2 is considered as small sized vortex particles, which has no feature for positive B_u along the vertical axis. A peak around $B_c = 0$ along the central ridge suggests the presence of superparamagnetic (SP) particles for specimens *o*1 and *o*2. C2 is associated with features along the central ridge on 20–80 mT, representing noninteracting SD particles.

Principal component analysis (FORC PCA) was conducted on the measured FORCs (Figure 5; Harrison et al., 2018). Three end-members EM1, EM2 and EM3 were recognized and their relative proportions in all specimens are plotted in Figures 6b and 10e. EM1 is representative of specimen *k*1 (surface), EM2 of specimen *l*1 (5 mm depth), and EM3 of specimen *o*1–*o*2 (center), respectively. Specimens other than *k*1, *o*1, and *o*2 are clustered close to specimen *l*1. FORC-PCA clearly resolves features characteristic to *o*1 and *o*2 (EM3). The central ridge is tailing from zero toward 100 mT (Figure 5i). The features around $B_c = 0$ may be due to superparamagnetic particles and those with higher coercivities are noninteracting SD particles. EM1 is separated as characteristic to *k*1 (Figure 5c), which has higher coercivity for the central ridge (25 mT; Figure 5g) compared with that of EM2 (20 mT; Figure 5h). Difference in vortex feature and its coercivity for EM1/EM2 and EM3 may reflect their grain sizes (~20 mT for 150–250 nm magnetite in Figure 8 of Almeida et al. (2015); 40–65 mT for 58 nm magnetite in Figure 22c of Roberts et al. (2014)) and/or oxidation states (Figure 8a of Almeida et al. (2015)).

C4 is assumed to be hematite based on the absence of unblocking temperatures near the Curie point of goethite (~120°C) during thermal demagnetization of composite IRM (Lowrie, 1990; Figure 6). The results of low temperature magnetometry are summarized in Figure 7. Recognition of Verwey transitions with low temperature magnetometry (Figure 8f) suggests the presence of magnetite/maghemite as well as the unblocking temperatures

Figure 2. Paleomagnetic results and an age model for the studied nodule. Vector endpoint diagrams for (a) B92-1-1-A-2-11 and (b) B92-1-1-B-2-b1. Solid (open) circles are projections onto horizontal (vertical) planes. Declinations and inclinations of high coercivity components along five lines for (c) Sample-A and (d) Sample-B. Declinations and inclinations plotted versus corrected depth for (e) Sample-A and (f) Sample-B. Corrected depths for five lines were calculated using growth layers for Sample-A and Sample-B (Figure S1 in Supporting Information S1). (g) Depth versus age plot for the four measured data based on $^{10}\text{Be}/^9\text{Be}$ method (black solid circles). Black broken lines represent interpolations between the adjacent age data points, assuming a linear change. The diagram suggests that the growth rate between 0 and 5 Ma (0.9 mm/Ma) is considerably lower than that between 5 and 8 Ma (5–7.5 mm/Ma). The bottom of the diagram is the geomagnetic polarity timescale (Ogg, 2020), where black and white represent normal, and reversed polarities, respectively. Horizontal and vertical red broken lines suggest expected age intervals for the specimens from line *k* of Sample-A.

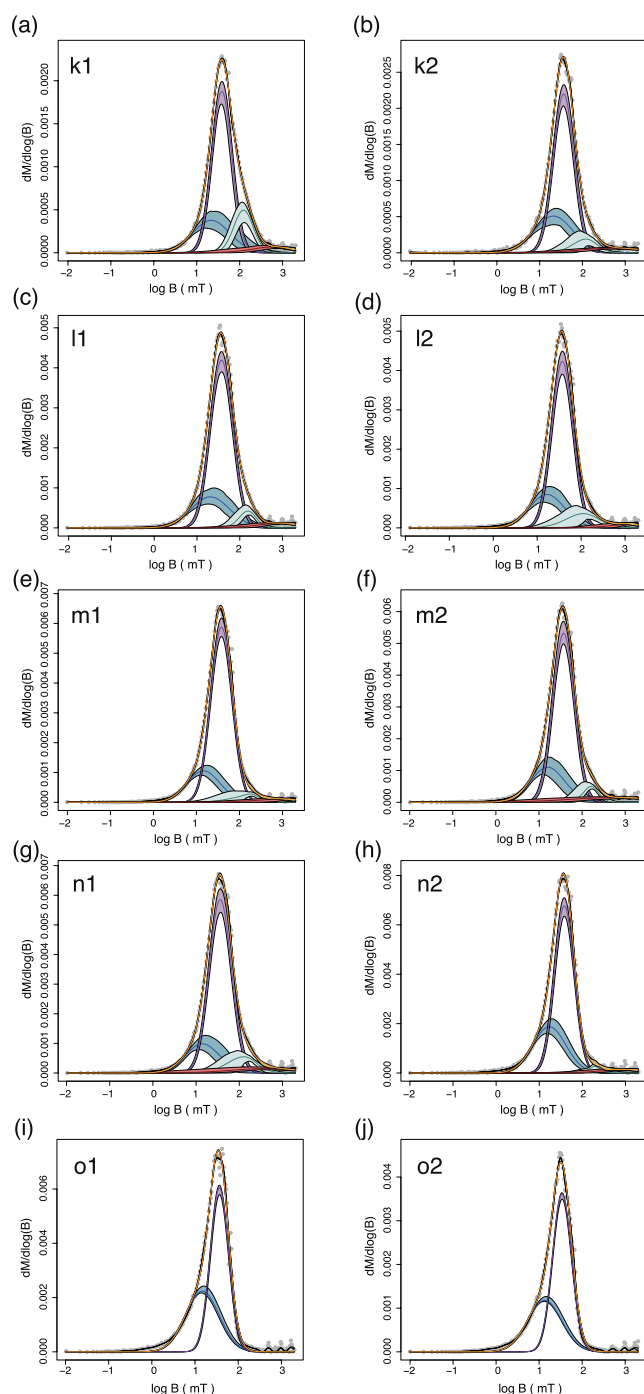


Figure 3. Isothermal remanent magnetization acquisition curves of specimens *k1*–*o2* for Sample-A decomposed into log-normal coercivity components using the *MaxUmix* software (Maxbauer et al., 2016). Four components are fitted for *k1*–*n2* (a–h), and two components for *o1*–*o2* (i–j). Color bands for each component represent 95% confidence limits.

up to $\sim 560^{\circ}\text{C}$ in the low coercivity components for the thermal demagnetization of the composite IRM.

The origin of these magnetic minerals could be biogenic magnetite, eolian dust, and/or detrital grains from upstream in the South Pacific and the surrounding area deposited and transported by deep currents. The 95% confidence limit (color bands in Figure 3) of C4 (interpreted as hematite) is well above zero and C4 is about 3%–6% of the total magnetization (Figure 9d). The contribution of hematite as weight (and volume) is quite significant considering that the mass specific moment of hematite is less than 1/100 of magnetite and maghemite.

Specimens *o1* and *o2* (17–21 mm; >7 Ma) have finer magnetic particles without hematite, suggesting a global or local climate change between specimens *o1* and *n2*. It is known that the late Miocene global cooling was initiated in the final stage of a long-term, global $\delta^{13}\text{C}$ decrease (Late Miocene Carbon Isotope Shift) at ~ 7 Ma (e.g., Steinthorsdottir et al., 2021). The initiation of global cooling is consistent with the timing of hematite observation in the nodule. Dunlea et al. (2015) analyzed pelagic sediments for the South Pacific Gyre, which is south of the studied area, and suggested Australia as the predominant source of dust. We suggest a possibility that the hematite might be included in the eolian dust, which could have been blown from Australia by the intensified wind after the initiation of global cooling at ~ 7 Ma and transported to the studied site. The increase in the grain size of magnetite/maghemite particles after ~ 7 Ma is also consistent with the idea of intensified wind blowing over Australia. Chemical changes after deposition may also have affected the magnetic mineralogy, as discussed in the following section.

4. Discussions

4.1. Oxidation of Magnetic Minerals

Although magnetic transitions are vague (Figure 7), the method of Jackson and Moskowitz (2021) enabled us to recognize Verwey transitions for magnetite (94–104 K; Figure 8f). They also summarized that the Verwey transition temperature is lowered by low temperature oxidation (nonstoichiometry) as well as impurities in the magnetite such as Ti, Al, or Mn. ΔM_c (Özdemir & Dunlop, 2010) decreases from ~ 0.05 ($Z = 0.89$; 89% oxidation) around the surface to ~ 0.01 ($Z = 0.975$; 97.5% oxidation) deeper in the nodule (Figure 8g). Verwey transition temperatures (94–104 K) lower than those of stoichiometric magnetite (125 K), subdued transitions, and low ΔM_c suggest low temperature oxidation of magnetite to maghemite. The absence of FORC features along the central ridge on 80–100 mT for specimens *o1* and *o2* (Figure 4) could be interpreted as lowered coercivity due to release of stress by the heavily or completely oxidized magnetite core surrounded by maghemite shell (e.g., Almeida et al., 2015). Specimen *k1* is characterized by higher coercivity for the central ridge (EM1; Figure 8e) reflecting SD magnetite with maghemite shell.

4.2. Nodule Rotation and Possible Causes

Changes in paleomagnetic directions for the five depth layers are almost synchronous from the bottom to the surface for Sample-B (Figures 9a–9e). The directional synchronicity for sample-A is not obvious. To visualize changes for Sample-B through time, the paleomagnetic directions were plotted for each line (Figures 9f–9j), where a great circle (GC) could be fitted

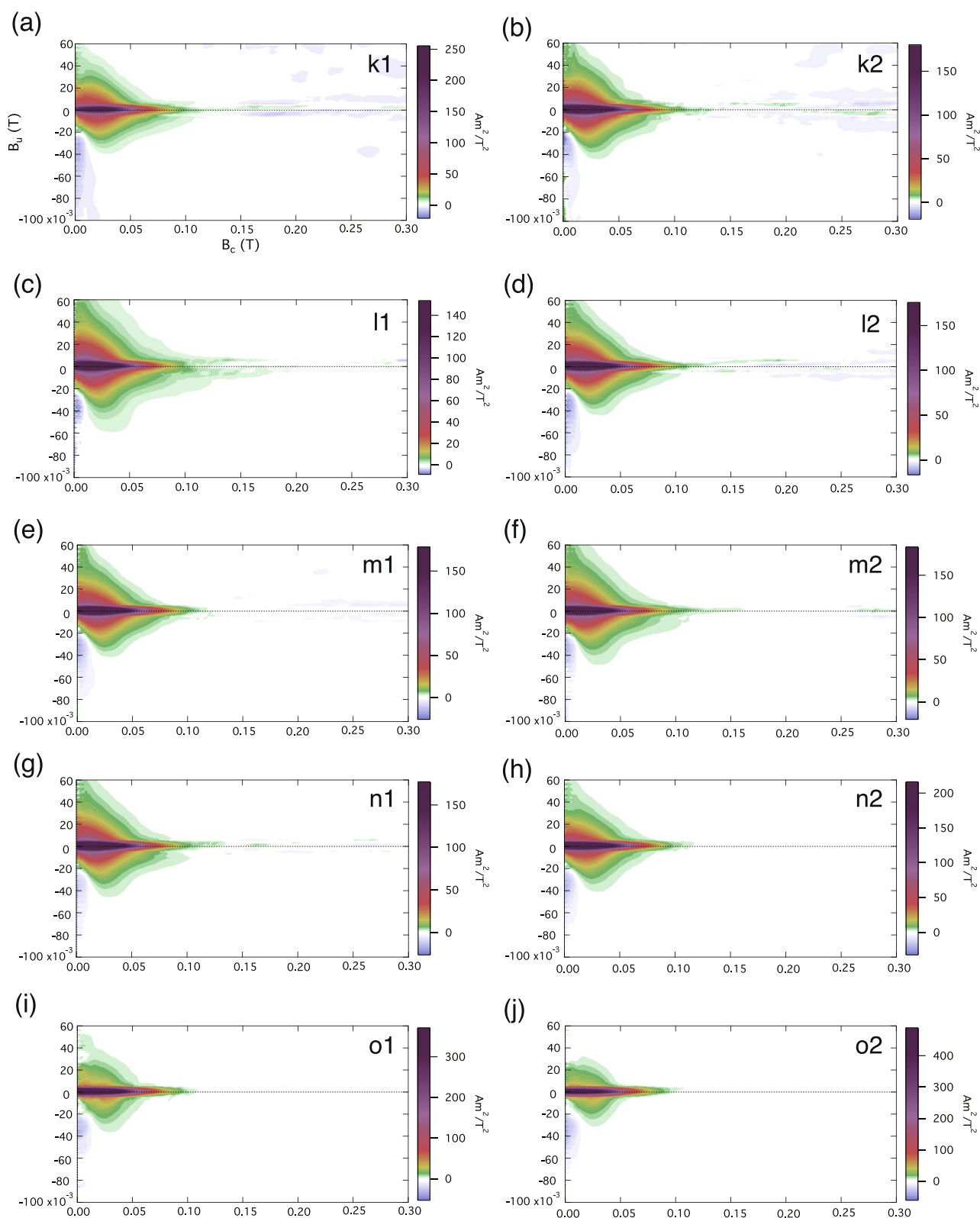


Figure 4. First-order reversal curve (FORC) diagrams for specimens *k1–o2* for Sample-A. FORC measurements were conducted with the following parameters; H_c : 0–400 mT, H_u : $-100 \sim +100$ mT, Saturation field: 2 T, Pause at saturation field: 0.1 s, Pause at calibration field: 0.1 s, Pause at reversal fields: 1 s, Number of FORCs: 150, Field step size: 4.027 mT, Averaging time: 0.4 s. FORC was processed using the *FORCinel* software (Harrison & Feinberg, 2008) with the following parameters; Sc_0 : 4, Sc_1 : 8, Sb_0 : 3, Sb_1 : 8, horizontal λ : 0.1, vertical λ : 0.1.

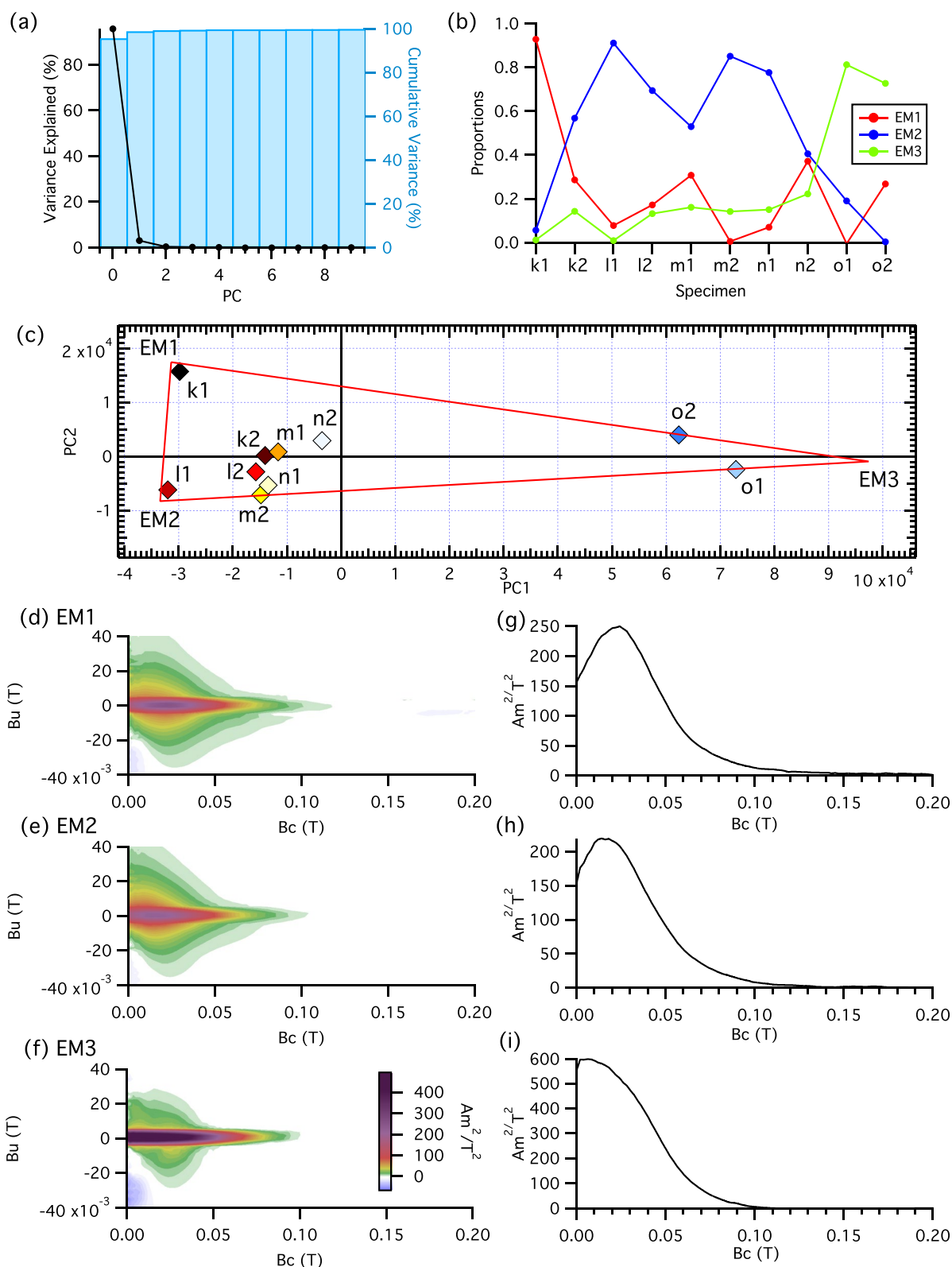


Figure 5. Results of first-order reversal curve (FORC) PCA. (a) Variance explained using principal components (solid circles) is shown together with cumulative variance (blue columns). (b) Proportions of end members EM1, EM2 and EM3 for specimens. (c) PC2 versus PC1 plotted for 10 specimens with the end members. FORC diagrams for (d) EM1, (e) EM2, and (f) EM3 sharing color scales. Horizontal profiles on FORC diagrams along $B_u = 0$ are shown for (g) EM1, (h) EM2, and (i) EM3.

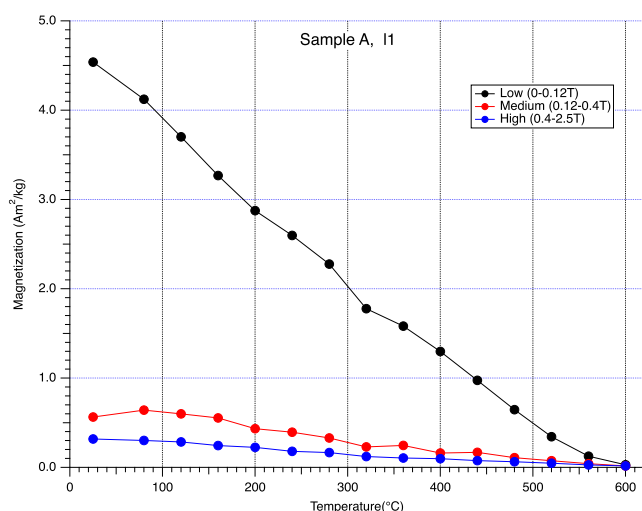


Figure 6. Results of thermal demagnetization of composite isothermal remanent magnetization (Lowrie, 1990) for specimen I1 of Sample-A. Black, red and blue circles represent magnetizations of low (0–0.12 T), medium (0.12–0.4 T) and high (0.4–2.5 T) coercivity components, respectively.

using PCA (Kirschvink, 1980). The consistency of the five GCs suggests that the nodule rotated while magnetization was acquired successively from the deepest layer 5 to the surface layers 1. The poles for the GCs give an average azimuth of $53.9 \pm 5.6^\circ$ and a dip of $32.1 \pm 7.6^\circ$ (Table 2). Directions could be reconstructed to the GAD field direction by progressive anticlockwise rotation (average rotation angle for the oldest specimens = $107.5 \pm 13.6^\circ$). This suggests that the nodule successively acquired magnetization during the last normal polarity period during rotation. The nodule might have rotated multiple times. Since there is no reversed magnetization preserved in the paleomagnetic records, the magnetization acquired during the previous rotations might have been erased.

There are potential causes for nodule rotation: (a) benthic macrofauna, (b) deep currents, and (c) gravity. The first hypothesis should exhibit sporadic directional changes. However, the directional change is rather continuous (Figures 9f–9j), which does not favor the hypothesis. The second hypothesis necessitates hydrostatic pressures to push the nodule; however, the speed of deep current in the area is not strong enough (a few cm/s; Thran et al., 2018). The paleomagnetic directions for a nodule from CCZ did not experience rotation (Yi et al., 2020). As the deep current speed for CCZ is similar to the studied area (Figure 1a; Kawabe & Fujio, 2010), it may not be a controlling factor for the rotation. The third hypothesis is the rotation along a gentle slope around the foot of an abyssal hill, where the nodule is located (Figure 1b;

Usui et al., 1994). Although the slope seems gentle, gradual nodule rotation due to gravity may be possible if the deep currents remove the sediments surrounding the nodule by episodic strong currents. Li et al. (2021) suggested that the nodules of the Suda Seamount in the northwest Pacific with 40%–80% areal coverage are associated with downslope movement, which provided the nucleus for high nodule concentrations. Although the scales and environments are different, their hypothesis gives ideas on the rotation of the nodule in the studied area with a high coverage of 57%. For a field of Co-rich manganese deposits on a seamount, the occurrences of large-scale nodules were favored for seabed slopes of $<3^\circ$ (Yamazaki & Sharma, 2000). Thus, it is possible that a gentle slope might be one of the important factors for the formation of large-scale nodules as well as the topographic features and the bottom currents.

4.3. Nodule Attitude and Remagnetization

Reconstructions of the nodule attitudes are made by the estimated rotation angle and axis (Figures 10a–10f). The rotation might have raised the northwest side of the nodule from the sediment and promoted low temperature oxidation of magnetite with seawater. Low temperature oxidation experiments on titanomagnetite bearing oceanic basalts demonstrated the acquisition of chemical remanent magnetization (CRM; Kelso et al., 1991). A model is proposed that primary magnetizations of magnetite were lost, and CRMs were acquired by oxidation (Fe^{2+} removal) associated with rotation (Figure 10g), where the magnetite core sizes were reduced to those smaller than the threshold. This applies to both SD and vortex particles (e.g., Almeida et al., 2015). The high oxidation degree (lowest ΔM_c for 17–21 mm; Figure 8g) might be related to the finer grain sizes of SP/SD/vortex particles with more reactive surfaces. Also, the segment around 17–21 mm might have been exposed longest (or most times) to the oxic seawater. The nodules for 0–17 mm contain larger sized vortex magnetites, which might have originated from eolian dust from Australia. The lack of these particles makes a strong contrast in terms of the average oxidation degree of magnetite particles. The higher oxidation degree for the segment around 17–19 mm does not necessarily mean that the speed of oxidation is higher than the outer part (0–17 mm).

The pores and cracks of the nodules (mean porosity is 43.0% for nodules from CCZ; Blöthe et al., 2015) connect the interior and the surrounding environment, introducing oxygenated seawater of AABW. Higher Mn is associated with hydrogenetic vernadite, which is correlated with lower Si (Figure 8h) and higher $S_{-0.1\text{ T}}$ (lower content of high coercivity minerals). This implies that oxidation proceeds more in areas with lower Mn and higher Si with sediments. Porous sediments (orange areas; Figure 10g) may have played a primary role as seawater pathways. The oxidation might have progressed from diagenetic parts with lower Mn and higher Si to the hydrogenetic columnar structure (purple areas; Figure 10g), which might have controlled the CRM acquisition resulting in

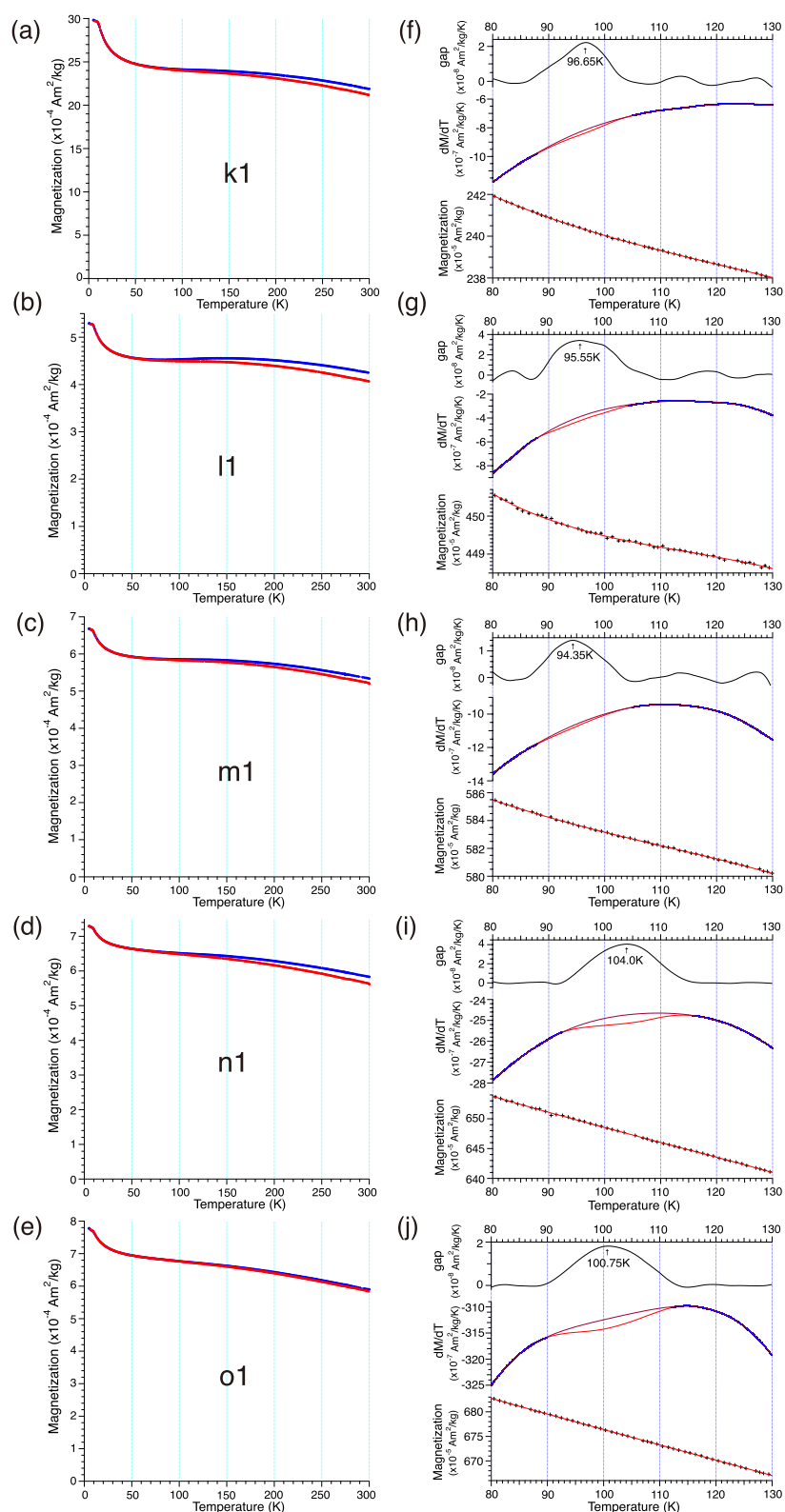


Figure 7.

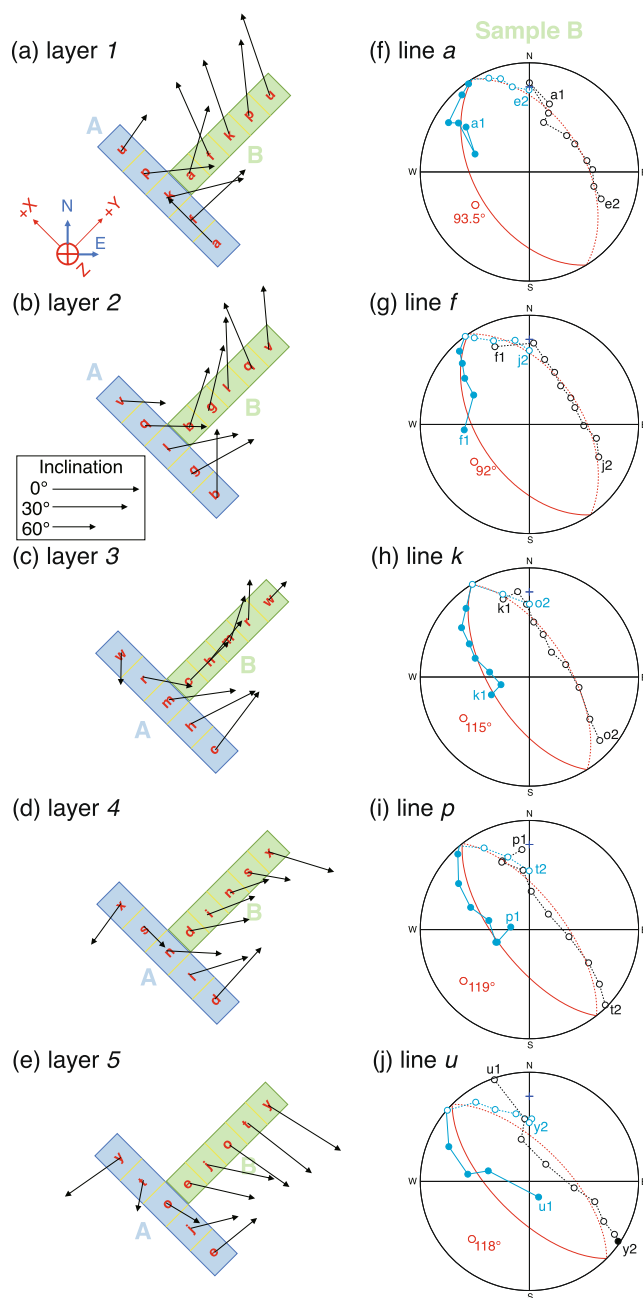


Figure 8. Rock magnetic results for specimens from line *k* of Sample-A. (a) SIRM. (b) $S_{-0.1T}$ and $S_{-0.3T}$. (c) Mean coercivities and (d) proportions of coercivity components for unmixing of isothermal remanent magnetization acquisition curves. (e) Proportions of first-order reversal curve end members. (f) Verwey transition temperatures and (g) ΔM_c . *Z* is the oxidation degree based on Özdemir and Dunlop (2010). (h) Optical image, Mn and Si XRF images, and $S_{-0.1T}$ enlarged images in the rectangles of Figure S2 in Supporting Information S1. An example area of sediment fillings and columnar vernadite are enclosed with white and cyan broken lines, respectively.

Figure 7. (a–e) Zero-field-cycling results of specimens *k1–o1* for Sample-A. Blue (red) points are cooling (warming) curves. (f–j) Verwey transition analyses proposed by Jackson and Moskowitz (2021). The ratio of reduction from warming to cooling curves at 300 K is calculated as ΔM_c based on Figures 6a–6e, which is associated with the degree of oxidation (Özdemir & Dunlop, 2010). For the lowest diagram of each subfigure, black crosses and red curves are the measured magnetization and interpolation using a smoothing spline, respectively. For the middle diagram of each subfigure, red, blue, and green curves represent the smoothed curve, data points used for polynomial fitting, and polynomial curve (term = 7) fitted using only blue data, respectively. The top diagram of each subfigure represents the subtraction of the smoothed curve from the polynomial curve, where the peak is the Verwey transition.

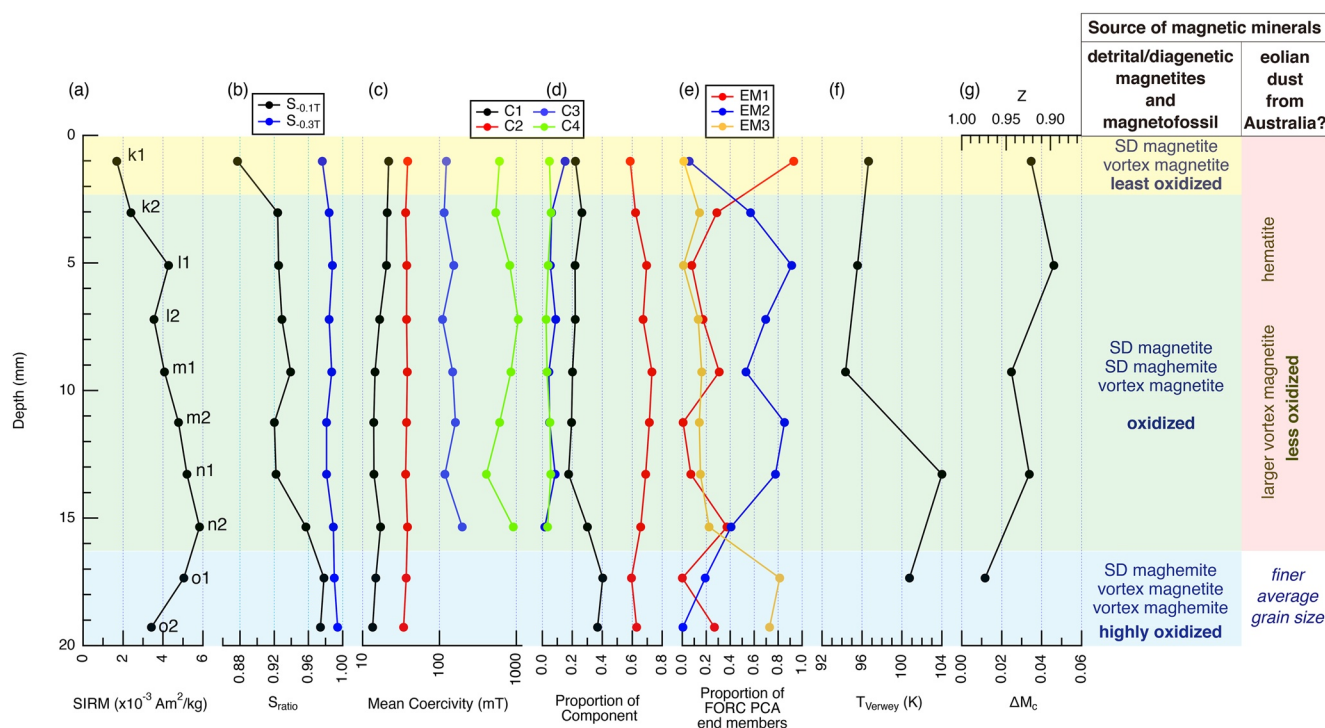
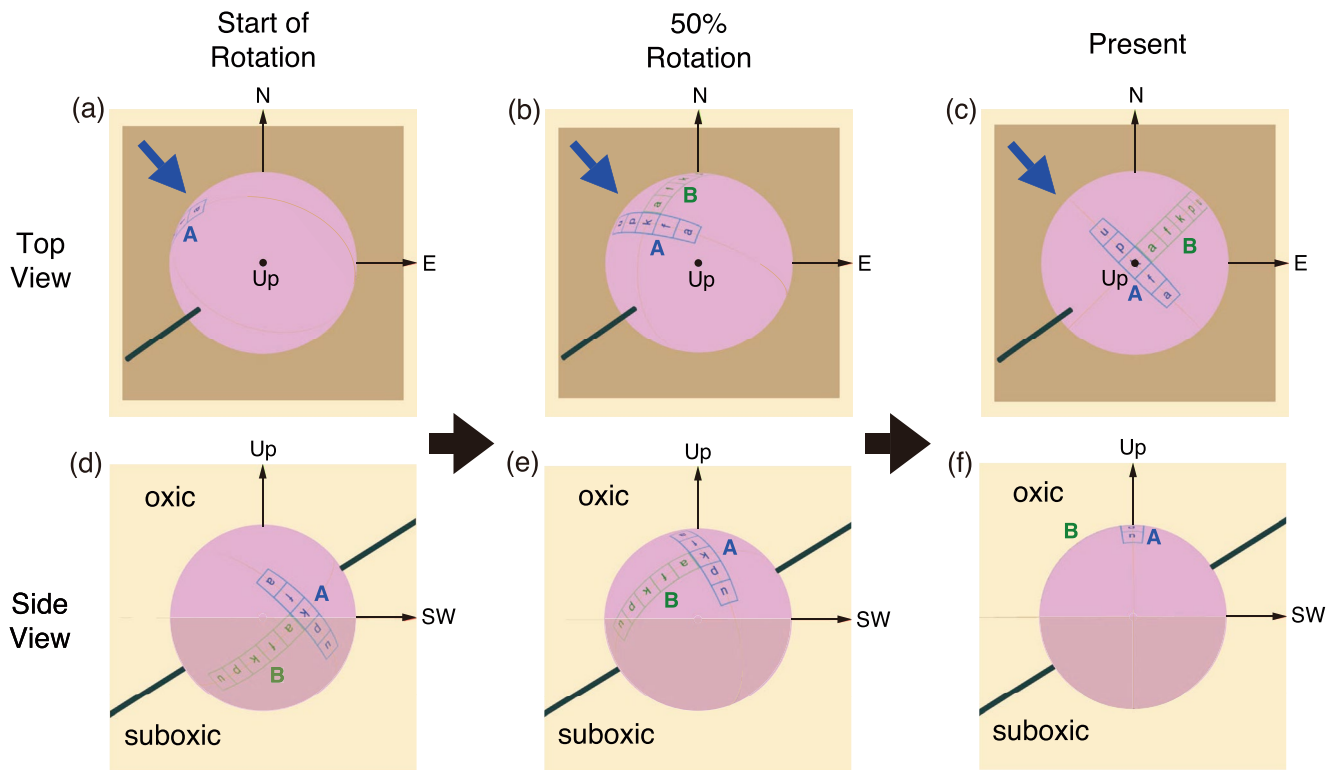


Figure 9. Paleomagnetic directions of layers (a) 1, (b) 2, (c) 3, (d) 4, and (e) 5 are shown as arrows after correction of -45° for the declination. Upper specimens were chosen for layers with two specimens. Blue and green rectangles are specimens for Sample-A and Sample-B, respectively. An angle from the north and a length for an arrow are declination and inclination, respectively. Solid arrows represent negative inclinations. Paleomagnetic directions for lines (f) a, (g) f, (h) k, (i) p, and (k) u for Sample-B are plotted as black circles on equal area projections. Blue crosses are the geocentric axial dipole field direction during the normal polarity period. Orange arcs and circles represent the GCs and the poles fitted to the directions, respectively. The numbers are rotation angles to restore the oldest specimen to zero declination. The restored paleomagnetic directions are plotted as cyan circles. Open (closed) circles are projections onto the upper (lower) hemisphere.

the complex distribution of paleomagnetic directions. pH might be important for the CRM acquisition (Kelso et al., 1991) as well as microbial activities in the nodule (Blöthe et al., 2015).

Throughout the life of the nodule from the beginning to the present, the central (deepest) part might have experienced rotations most times and the lifetime number of rotations of the segment may decrease toward its surface. Considering the fact that the reversed magnetization is not recorded in the specimens, every time a certain segment of the nodule experiences a suboxic condition below the sediment water interface, the magnetization



(g) Schematic cross section of the nodule and possible CRM acquisition mechanism

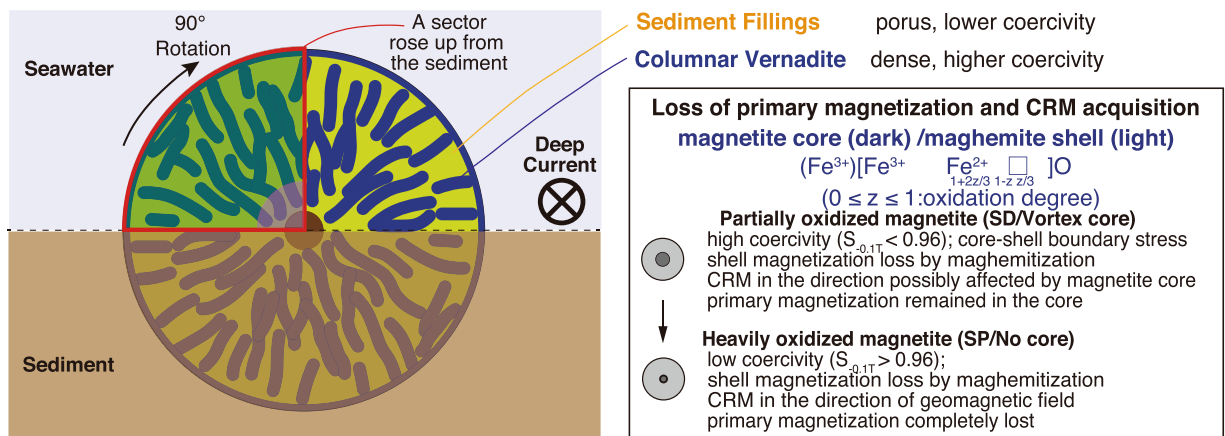


Figure 10. The attitude of the nodule during rotation with a rotation angle of 107.5° along an axis (azimuth = 53.9° , dip = 32.1°) based on the average for Sample-B. Upper subfigures are top views of the nodule (a) before, and after (b) 50%, and (c) 100% rotation. Lower subfigures (d–f) are the corresponding side views from northwest. The axis of rotation is shown as a thick black line. (d) Schematic cross section of a nodule after 90° rotation with a magnetization acquisition model. The rotation axis is simplified as horizontal. The CRM acquisition model is shown in the boxes.

that has been acquired in the previous oxic stage above the sediment water interface might have been lost due to chemical change or dissolution. When the segment is above the sediment water interface, the oxic seawater may enter from the upstream side of the outer part of the nodule, then move to the central (deepest) part, and finally go out from the downstream side of the outer part. Assuming that the deep current is flowing from southwest to northeast, Sample B is located on the upper part of the downstream side of the nodule. Then, the successive acquisition of magnetization from the deepest layer 5 (upstream) to the surface layers 1 (downstream) is considered as consistent with the above interpretation.

Table 2
Poles of Great Circles and Rotation Angles for Five Lines of Sample-B

Lines of sample-B	Pole of great circle			Rotation angle (°)
	Direction (°)	Dip (°)	MAD (°)	
Line <i>a</i>	−121.4	−41.5	10.8	93.5
Line <i>f</i>	−124.0	−38.8	9.0	92
Line <i>k</i>	−122.0	−29.5	8.7	115
Line <i>p</i>	−127.9	−24.4	11.6	119
Line <i>u</i>	−135.0	−26.4	19.2	118
Average	−126.1	−32.1	11.9	107.5
Std Dev	5.6	7.6	-	13.6

5. Conclusions

Paleomagnetic measurements were made on specimens cut from a nodule with depth recovered from the Penrhyn Basin, South Pacific. A stable normal polarity magnetization has been resolved from each specimen. The direction for the surface specimen is consistent with the recent geomagnetic fields, whereas paleomagnetic directions show systematic differences among the specimens forming a GC with a pole at (azimuth = 53.9°, dip = 32.1°). The nodule might have acquired CRM during the normal polarity period while undergoing rotation. A possible mechanism for the rotation of the nodule is downslope rolling assisted by sediment removal by a deep current. The rotation might have changed the pore water condition to oxidative for the rising part of the nodule, which might have led to low temperature oxidation of magnetite causing CRM acquisition. The rotation facilitates the growth of a mixed layer of diagenetic buserite and hydrogenetic vernadite, which influences the elements in the nodule as natural resources.

Conflict of Interest

The authors declare no conflicts of interest relevant to this study.

Data Availability Statement

The data can be accessed at <https://doi.org/10.5281/zenodo.7592334>.

Acknowledgments

The authors thank Y. Yamauchi, E. Miyamura, A. Katayama, Y. Harigane, and B. Dordill for the measurements. The authors express sincere thanks to two reviewers, Brendan Cyth and Tilo von Dobeneck, and an editor, Joshua Feinberg. Kochi Core Center Grant 21A034/21B032 supported MPMS measurements. HO was supported by JSPS KAKENHI Grant 20KK0082/21H04523.

References

- Almeida, T. P., Muxworthy, A. R., Kasama, T., Williams, W., Damsgaard, C., Frandsen, C., et al. (2015). Effect of maghemization on the magnetic properties of nonstoichiometric pseudo-single-domain magnetite particles. *Geochemistry, Geophysics, Geosystems*, 16(9), 2969–2979. <https://doi.org/10.1002/2015GC005858>
- Bloemendal, J., King, J. W., Hall, F. R., & Doh, S.-J. (1992). Rock magnetism of Late Neogene and Pleistocene deep-sea sediments: Relationship to sediment source, diagenetic processes and sediment lithology. *Journal of Geophysical Research*, 97(B4), 4361–4375. <https://doi.org/10.1029/91JB03068>
- Blöthe, M., Węgorzewski, A., Müller, C., Simon, F., Kuhn, T., & Schippers, A. (2015). Manganese-cycling microbial communities inside deep-sea manganese nodules. *Environmental Science and Technology*, 49(13), 7692–7700. <https://doi.org/10.1021/es504930v>
- Chmieleff, J., von Blanckenburg, F., Kossert, K., & Jakob, D. (2010). Determination of the ¹⁰Be half-life by multicollector ICP-MS and liquid scintillation counting. *Nuclear Instruments and Methods in Physics Research B*, 268(2), 192–199. <https://doi.org/10.1016/j.nimb.2009.09.012>
- Dunlea, A. G., Murray, R. W., Sauvage, J., Spivack, A. J., Harris, R. N., & D'Hondt, S. (2015). Dust, volcanic ash, and the evolution of the South Pacific Gyre through the Cenozoic. *Paleoceanography*, 30(8), 1078–1099. <https://doi.org/10.1002/2015PA002829>
- Dutkiewicz, A., Judge, A., & Müller, R. D. (2020). Environmental predictors of deep-sea polymetallic nodule occurrence in the global ocean. *Geology*, 48(3), 293–297. <https://doi.org/10.1130/G46836.1>
- Graham, I. J., Carter, R. M., Ditchburn, R. G., & Zondervan, A. (2004). Chronostratigraphy of ODP 181, Site 1121 sediment core (Southwest Pacific Ocean), using ¹⁰Be/⁹Be dating of entrapped ferromanganese nodules. *Marine Geology*, 205(1–4), 227–247. [https://doi.org/10.1016/S0025-3227\(04\)00025-8](https://doi.org/10.1016/S0025-3227(04)00025-8)
- Harrison, R. J., & Feinberg, J. M. (2008). FORCinel: An improved algorithm for calculating first-order reversal curve distributions using locally weighted regression smoothing. *Geochemistry, Geophysics, Geosystems*, 9(5), Q05016. <https://doi.org/10.1029/2008GC001987>
- Harrison, R. J., Muraszko, J., Heslop, D., Lascu, I., Muxworthy, A. R., & Roberts, A. P. (2018). An improved algorithm for unmixing first-order reversal curve diagrams using principal component analysis. *Geochemistry, Geophysics, Geosystems*, 19(5), 1595–1610. <https://doi.org/10.1029/2018GC007511>
- Jackson, M. J., & Moskowitz, B. (2021). On the distribution of Verwey transition temperatures in natural magnetites. *Geophysical Journal International*, 224(2), 1314–1325. <https://doi.org/10.1093/gji/ggaa516>
- Jiang, X. D., Zhao, X., Chou, Y. M., Liu, Q. S., Roberts, A. P., Ren, J. B., et al. (2020). Characterization and quantification of magnetofossils within abyssal manganese nodules from the Western Pacific Ocean and implications for nodule formation. *Geochemistry, Geophysics, Geosystems*, 21(3), e2019GC008811. <https://doi.org/10.1029/2019GC008811>
- Jiang, X. D., Zhao, X., Zhao, X. Y., Chou, Y.-M., Roberts, A. P., Hein, J. R., et al. (2022). Abyssal manganese nodule recording of global cooling and Tibetan Plateau uplift impacts on Asian aridification. *Geophysical Research Letters*, 49(3), e2021GL096624. <https://doi.org/10.1029/2021GL096624>
- Joshima, M., & Usui, A. (1998). Magnetostratigraphy of hydrogenetic manganese crusts from Northwestern Pacific seamounts. *Marine Geology*, 146(1–4), 53–62. [https://doi.org/10.1016/S0025-3227\(97\)00131-X](https://doi.org/10.1016/S0025-3227(97)00131-X)
- Kawabe, M., & Fujio, S. (2010). Pacific Ocean circulation based on observation. *Journal of Oceanography*, 66(3), 389–403. <https://doi.org/10.1007/s10872-010-0034-8>

- Kawai, J., Oda, H., Fujihira, J., Miyamoto, M., Miyagi, I., & Sato, M. (2016). SQUID microscope with hollow-structured cryostat for magnetic field imaging of room temperature samples. *IEEE Transactions on Applied Superconductivity*, 26(5), 1–5. <https://doi.org/10.1109/TASC.2016.2536751>
- Kelso, P. R., Banerjee, S. K., & Worm, H.-U. (1991). The effect of low-temperature hydrothermal alteration on the remanent magnetization of synthetic titanomagnetites: A case for acquisition of chemical remanent magnetization. *Journal of Geophysical Research*, 96(B12), 19545–19553. <https://doi.org/10.1029/91JB01975>
- Kirschvink, J. L. (1980). The least-squares line and plane and the analysis of palaeomagnetic data. *Geophysical Journal of the Royal Astronomical Society*, 62(3), 699–718. <https://doi.org/10.1111/j.1365-246X.1980.tb02601.x>
- Korschinek, G., Bergmaier, A., Faestermann, T., Gerstmann, U. C., Knie, K., Rugel, G., et al. (2010). A new value for the half-life of ^{10}Be by heavy-ion elastic recoil detection and liquid scintillation counting. *Nuclear Instruments and Methods in Physics Research B*, 268(2), 187–191. <https://doi.org/10.1016/j.nimb.2009.09.020>
- Koymans, M. R., van Hinsbergen, D. J. J., Pastor-Galan, D., Vaes, B., & Langereis, C. G. (2020). Towards FAIR paleomagnetic data management through Paleomagnetism.org 2.0. *Geochemistry, Geophysics, Geosystems*, 21(2), e2019GC008838. <https://doi.org/10.1029/2019GC008838>
- Li, Z., Li, H., Hein, J. R., Dong, Y., Wang, M., Ren, X., et al. (2021). A possible link between seamount sector collapse and manganese nodule occurrence in the abyssal plains, NW Pacific Ocean. *Ore Geology Reviews*, 138, 104378. <https://doi.org/10.1016/j.oregeorev.2021.104378>
- Lowrie, W. (1990). Identification of ferromagnetic minerals in a rock by coercivity and unblocking temperature properties. *Geophysical Research Letters*, 17(2), 159–162. <https://doi.org/10.1029/GL017i002p00159>
- Maxbauer, D. P., Feinberg, J. M., & Fox, D. L. (2016). MAX UnMix: A web application for unmixing magnetic coercivity distributions. *Computers & Geosciences*, 95, 140–145. <https://doi.org/10.1016/j.cageo.2016.07.009>
- Müller, R. D., Cannon, J., Qin, X., Watson, R. J., Gurnis, M., Williams, S., et al. (2018). GPlates: Building a virtual Earth through deep time. *Geochemistry, Geophysics, Geosystems*, 19(7), 2243–2261. <https://doi.org/10.1029/2018GC007584>
- Nishimura, A., & Saito, Y. (1994). IV. Deep-sea sediments in the Penrhyn Basin, South Pacific (GH83-3 Area). *Geological Survey of Japan Cruise Report*, 23, 41–60.
- Noguchi, A., Oda, H., Yamamoto, Y., Usui, A., Sato, M., & Kawai, J. (2017). Scanning SQUID microscopy of a ferromanganese crust from the northwestern Pacific: Submillimeter scale magnetostratigraphy as a new tool for age determination and mapping of environmental magnetic parameters. *Geophysical Research Letters*, 44(11), 5360–5367. <https://doi.org/10.1002/2017GL073201>
- Oda, H., Kawai, J., Miyamoto, M., Miyagi, I., Sato, M., Noguchi, A., et al. (2016). Scanning SQUID microscope system for geological samples: System integration and initial evaluation. *Earth Planets and Space*, 68(1), 179. <https://doi.org/10.1186/s40623-016-0549-3>
- Oda, H., Kawai, J., Usui, A., Yamamoto, Y., Noguchi, A., Miyagi, I., et al. (2020). Development of scanning SQUID microscope system and its applications on geological samples: A case study on marine ferromanganese crust. *Journal of Physics: Conference Series*, 1590(1), 012037. <https://doi.org/10.1088/1742-6596/1590/1/012037>
- Oda, H., Nakasato, Y., & Usui, A. (2018). Characterization of marine ferromanganese crust from the Pacific using residues of selective chemical leaching: Identification of fossil magnetotactic bacteria with FE-SEM and rock magnetic methods. *Earth Planets and Space*, 70(1), 165. <https://doi.org/10.1186/s40623-018-0924-3>
- Oda, H., Usui, A., Miyagi, I., Joshima, M., Weiss, B. P., Shantz, C., et al. (2011). Ultrafine-scale magnetostratigraphy of marine ferromanganese crust. *Geology*, 39(3), 227–230. <https://doi.org/10.1130/G31610.1>
- Ogg, J. G. (2020). Chapter 5-geomagnetic polarity time scale. In F. M. Gradstein, J. G. Ogg, M. D. Schmitz, & G. M. Ogg (Eds.), *Geologic time scale 2020* (pp. 159–192). Elsevier. <https://doi.org/10.1016/B978-0-12-824360-2.00005-X>
- Özdemir, Ö., & Dunlop, D. J. (2010). Hallmarks of maghemitization in low-temperature remanence cycling of partially oxidized magnetite nanoparticles. *Journal of Geophysical Research*, 115(B2), B02101. <https://doi.org/10.1029/2009JB006756>
- Roberts, A. P., Heslop, D., Zhao, X., & Pike, C. R. (2014). Understanding fine magnetic particle systems through use of first-order reversal curve diagrams. *Reviews of Geophysics*, 52(4), 557–602. <https://doi.org/10.1002/2014RG000462>
- Skowronek, A., Maciag, Ł., Zawadzki, D., Strzelecka, A., Baláz, P., Mianowicz, K., et al. (2021). Chemostratigraphic and textural indicators of nucleation and growth of polymetallic nodules from the Clarion-Clipperton fracture zone (IOM Claim area). *Minerals*, 11(8), 868. <https://doi.org/10.3390/min11080868>
- Steinthorsdóttir, M., Coxall, H. K., de Boer, A. M., Huber, M., Barbolini, N., Bradshaw, C. D., et al. (2021). The Miocene: The future of the past. *Paleoceanography and Paleoclimatology*, 36(4), e2020PA004037. <https://doi.org/10.1029/2020PA004037>
- Thran, A. C., Dutkiewicz, A., Spence, P., & Müller, R. D. (2018). Controls on the global distribution of contourite drifts: Insights from an eddy-resolving ocean model. *Earth and Planetary Science Letters*, 489, 228–240. <https://doi.org/10.1016/j.epsl.2018.02.044>
- Tozer, B., Sandwell, D. T., Smith, W. H. F., Olson, C., Beale, J. R., & Wessel, P. (2019). Global bathymetry and topography at 15 arc sec: SRTM15+. *Earth and Space Science*, 6(10), 1847–1864. <https://doi.org/10.1029/2019EA000658>
- Usui, A. (1979). Minerals, metal contents, and mechanism of formation of manganese nodules from the Central Pacific Basin (GH76-1 and GH77-1 areas). In J. L. Bischoff & D. Z. Piper (Eds.), *Marine Geology and Oceanography of the Pacific Manganese Nodule Provinces* (pp. 651–679). Plenum.
- Usui, A., & Ito, T. (1994). Fossil manganese deposits buried within DSDP/ODP cores, Legs 1–126. *Marine Geology*, 119(1–2), 111–136. [https://doi.org/10.1016/0025-3227\(94\)90144-9](https://doi.org/10.1016/0025-3227(94)90144-9)
- Usui, A., Mellin, T. A., Nohara, M., & Yuasa, M. (1989). Structural stability of marine 10 Å manganates from the Ogasawara (Bonin) Arc: Implication for low-temperature hydrothermal activity. *Marine Geology*, 86(1), 41–56. [https://doi.org/10.1016/0025-3227\(89\)90017-0](https://doi.org/10.1016/0025-3227(89)90017-0)
- Usui, A., Nishimura, A., & Mita, N. (1993). Composition and growth history of surficial and buried manganese nodules in the Penrhyn Basin, Southwestern Pacific. *Marine Geology*, 114(1–2), 133–153. [https://doi.org/10.1016/0025-3227\(93\)90044-V](https://doi.org/10.1016/0025-3227(93)90044-V)
- Usui, A., Nohara, M., Okuda, Y., Nishimura, A., Yamazaki, T., Saito, Y., et al. (1994). Outline of the cruise GH83-3 in the Penrhyn Basin, South Pacific. *Geological Survey of Japan Cruise Report*, 23, 1–17.
- Usui, A., & Someya, M. (1997). Distribution and composition of marine hydrogenetic and hydrothermal manganese deposits in the northwest Pacific. In K. Nicholson, J. R. Hein, B. Bühn, & S. Dasgupta (Eds.), *Manganese mineralization: geochemistry and mineralogy of terrestrial and marine deposits* (Vol. 119, pp. 177–198). Geological Society of London Special Publications.
- Verlaan, P. A., & Cronan, D. S. (2022). Origin and variability of resource-grade marine ferromanganese nodules and crusts in the Pacific Ocean: A review of biogeochemical and physical controls. *Geochemistry*, 82(1), 125741. <https://doi.org/10.1016/j.chemer.2021.125741>
- von Stackelberg, U. (1984). Significance of benthic organisms for the growth and movement of manganese nodules, Equatorial North Pacific. *Geo-Marine Letters*, 4(1), 37–42. <https://doi.org/10.1007/bf02237972>
- von Stackelberg, U. (2000). Manganese nodules of the Peru Basin (Chapter 8). In U. von Stackelberg & D. S. Cronan (Eds.), *Handbook of marine mineral deposits* (p. 424). <https://doi.org/10.1201/9780203752760>

- Weiss, B. P., Lima, E. A., Fong, L. E., & Baudenbacher, F. J. (2007). Paleomagnetic analysis using SQUID microscopy. *Journal of Geophysical Research*, 112(B9), B09105. <https://doi.org/10.1029/2007JB004940>
- Wessel, P., Luis, J. F., Uieda, L., Scharroo, R., Wobbe, F., Smith, W. H. F., & Tian, D. (2019). The generic mapping tools version 6. *Geochemistry, Geophysics, Geosystems*, 20(11), 5556–5564. <https://doi.org/10.1029/2019GC008515>
- Yamazaki, T., & Sharma, R. (2000). Morphological features of Co-rich manganese deposits and their relation to seabed slopes. *Marine Georesources and Geotechnology*, 18(1), 43–76. <https://doi.org/10.1080/10641190009353782>
- Yi, L., Medina-Elizalde, M., Kletetschka, G., Yao, H., Simon, Q., Paterson, G. A., et al. (2020). The potential of marine ferromanganese nodules from Eastern Pacific as recorders of Earth's magnetic field changes during the past 4.7 Myr: A geochronological study by magnetic scanning and authigenic $^{10}\text{Be}/^9\text{Be}$ dating. *Journal of Geophysical Research: Solid Earth*, 125(7), e2019JB018639. <https://doi.org/10.1029/2019JB018639>
- Yuan, W., Zhou, H., Yang, Z., Hein, J. R., & Yang, Q. (2020). Magnetite magnetofossils record biogeochemical remanent magnetization in hydrogenetic ferromanganese crusts. *Geology*, 48(3), 298–302. <https://doi.org/10.1130/G46881.1>
- Yuan, W., Zhou, H., Zhao, X., Yang, Z., Yang, Q., & Zhu, B. (2017). Magnetic stratigraphic dating of marine hydrogenetic ferromanganese crusts. *Scientific Reports*, 7(1), 16748. <https://doi.org/10.1038/s41598-017-17077-8>

Erratum

In the originally published version of this article, Figures 6 and 7 were transposed. Also, in the first line of Section 2.1, the geographic coordinates were incorrectly provided as “158.39°64’W, 12°00’03”S; Water depth: 5,248 m.” The figures have been updated to reflect the correct order, and the geographic coordinates have been updated to “158°30.64’W, 12°00.03’S; Water depth: 5,248 m.” This may now be considered the authoritative version of record.